Signatures of Quantized Energy States in Solution-Processed Ultrathin Layers of Metal-Oxide Semiconductors and Their Devices

John G. Labram, Yen-Hung Lin, Kui Zhao, Ruipeng Li, Stuart R. Thomas, James Semple, Maria Androulidaki, Lamprini Sygellou, Martyn McLachlan, Emmanuel Stratakis, Aram Amassian, and Thomas D. Anthopoulos**

Physical phenomena such as energy quantization have to-date been overlooked in solution-processed inorganic semiconducting layers, owing to heterogeneity in layer thickness uniformity unlike some of their vacuum-deposited counterparts. Recent reports of the growth of uniform, ultrathin (<5 nm) metal-oxide semiconductors from solution, however, have potentially opened the door to such phenomena manifesting themselves. Here, a theoretical framework is developed for energy quantization in inorganic semiconductor layers with appreciable surface roughness, as compared to the mean layer thickness, and present experimental evidence of the existence of quantized energy states in spin-cast layers of zinc oxide (ZnO). As-grown ZnO layers are found to be remarkably continuous and uniform with controllable thicknesses in the range 2–24 nm and exhibit a characteristic widening of the energy bandgap with reducing thickness in agreement with theoretical predictions. Using sequentially spin-cast layers of ZnO as the bulk semiconductor and quantum well materials, and gallium oxide or organic self-assembled monolayers as the barrier materials, two terminal electronic devices are demonstrated, the current–voltage characteristics of which resemble closely those of double-barrier resonant-tunneling diodes. As-fabricated all-oxide/hybrid devices exhibit a characteristic negative-differential conductance region with peak-to-valley ratios in the range 2–7.

1. Introduction

Solution-processed metal-oxide semiconductors[1,2] offer great promise for low-cost, large-area electronics and are currently the focus of great academic and commercial interest.[3] In the past few years significant progress has been made in reducing the processing temperature of high-performance solution processable metal-oxide semiconductors and devices,[4,5] traditionally a significant technological hurdle for this family of semiconductors. Furthermore, the growth of highly uniform and ultrathin (<5 nm) films of polycrystalline zinc oxide (ZnO) has also been demonstrated from solution at low temperatures (180 °C) leading to the realization of thin-film transistors (TFTs) with field-effect mobilities in excess of 10 $cm^2\ V s^{-1}$.[6] While the effect of channel thickness has recently been considered in solution-processed metal-oxide transistors,[7] work has thus far focused upon the impact of the channel dimensions on the electrical stability of

Dr. J. G. Labram, Y.-H. Lin, Dr. S. R. Thomas, J. Semple, Prof. T. D. Anthopoulos
Department of Physics
Blackett Laboratory
Imperial College London
London SW7 2AZ, UK
E-mail: j.labram@imperial.ac.uk; t.anthopoulos@imperial.ac.uk

Y.-H. Lin
Dutch Polymer Institute (DPI)
P. O. Box 902, 5600, AX, Eindhoven, The Netherlands

Dr. K. Zhao, Prof. A. Amassian
Materials Science and Engineering
Division of Physical Sciences and Engineering
King Abdullah University of Science and Technology
Thuwal 23955–6900, Saudi Arabia

Dr. R. Li
Cornell High Energy Synchrotron Source
Cornell University
Ithaca, NY 14850, USA

Dr. M. Androulidaki, Dr. L. Sygellou, Dr. E. Stratakis
Foundation for Research and Technology Hellas (FORTH)
Institute of Electronic Structure and Lasers (IESL)
Heraklion Crete and Institute of Chemical Engineering Sciences (ICEHT)
Patras, Greece

Dr. M. McLachlan
Department of Materials
Royal School of Mines
Imperial College London
London SW7 2AZ, UK

DOI: 10.1002/adfm.201403862

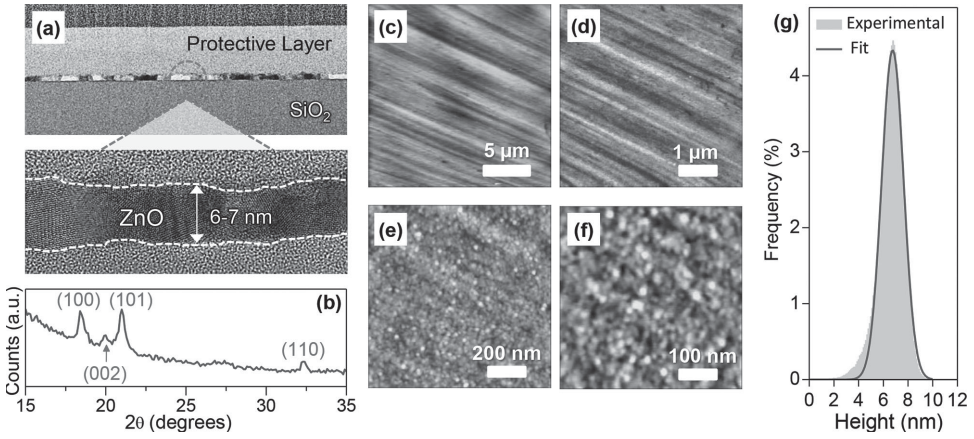

Figure 1. a) High-resolution transmission electron microscope (HRTEM) cross-sectional images (medium and high magnification) of a ZnO layer spin-coated on SiO_2. b) Grazing incident X-ray diffraction (GID) spectra of similar ZnO film on SiO_2 substrate. c–f) Tapping-mode atomic force microscopy (AFM) images of thin ZnO film deposited onto quartz substrate. g) Surface height distribution extracted from the AFM image in e). The solid line is a Gaussian distribution fitted to the experimental distribution, with a mean of 6.8 nm and a standard deviation of 0.9 nm.

the devices rather than on the possibility of forming quantized carrier states. Traditional semiconductor systems such as GaAs/AlGaAs deposited via sophisticated growth techniques, such as chemical vapor deposition (CVD) or molecular-beam epitaxy (MBE), are known to exhibit quantized sub-bands when carriers are confined in potential wells of dimensions below 5–10 nm.[8] Unlike traditional inorganic systems, however, solution-deposited oxide semiconducting layers are characterized by rough surfaces with root-mean-square (rms) roughness often on the order of several nanometers.[9] This characteristic combined with the amorphous/polycrystalline nature of most semiconducting oxides, has generally led to this family of materials being overlooked for use in low-dimensional devices. However, regardless of whether the system is smooth or rough or whether the transport of carriers in the semiconducting layer is described by a hopping-like or a band-like mechanism, if carriers are spatially confined in one dimension, the Schrödinger equation dictates that the energies available to these carriers will be restricted to quantized energy levels rather than a continuum.[10] Therefore, ultrathin metal-oxide semiconducting layers grown from solution at low temperatures could potentially provide an ideal test-bed for studying the possible formation of quantized carrier states.

In this work, we study the formation of quantized energy levels in ultrathin layers of ZnO processed from solution at 200 °C in ambient air. By tuning the molarity of the aqueous precursor solution and the spin-speed during deposition, growth of conformal, polycrystalline ZnO layers with controllable thicknesses in the range 2–24 nm, is demonstrated. By means of optical absorption and photoluminescent spectroscopy, we studied the impact of layer thickness on the optical properties of ZnO. Obtained results revealed a characteristic widening of the semiconductor bandgap in agreement with theoretical predictions for energy level quantization below a critical layer thickness. Further supporting evidence for the existence of quantized energy states in ultrathin ZnO layers, were obtained via electrical characterization of quantum-well structures based on all-oxide as well as on metal oxide/organic hybrid materials combinations.

2. Deposition of Ultrathin ZnO Layers from Solution

Recently[6,11] we demonstrated the ability to deposit ultrathin, highly uniform films of semiconducting ZnO by spin-casting from an aqueous ZnO precursor solution followed by a thermal annealing step at ≈180 °C. By employing various precursor concentrations and spinning speeds, the process has been employed here to produce ZnO films with mean thicknesses in the range 2–24 nm. In **Figure 1**a we show a high-resolution transmission electron microscope (HRTEM) cross-sectional image of a solution-processed ZnO film on a SiO_2 substrate at two different magnifications. The film is found to be visibly polycrystalline with a mean thickness of approximately 6.5 nm. In Figure 1b we show a grazing incident X-ray diffraction (GID) spectrum of a ZnO layer processed under identical conditions, again indicating a randomly oriented polycrystalline structure.

Tapping-mode atomic force microscopy (AFM) images of a similar film deposited onto quartz are displayed in Figure 1c–f. In the large-area scan images of Figure 1c,d), clear straight lines-like features are observed. These are attributed to the drying of the precursor solution in the presence of centrifugal forces during spin-casting. Although the film is generally continuous, small voids can be observed in the highest magnification images of Figure 1e,f, which are believed to show the surface of the quartz substrate. By assuming that the AFM tip makes physical contact with the substrate surface at least once during the full scan, one can extract the height-profile of the ZnO layer directly from these AFM images and accurately assess the degree of substrate coverage. In Figure 1g we show the experimental film thickness height distribution extracted from the AFM image of Figure 1e, fitted to a Gaussian distribution with a mean thickness of 6.8 nm and standard deviation of 0.9 nm. This is in good agreement with the HRTEM image of Figure 1a as well as further HRTEM images taken for various ZnO layers with different thicknesses. Field-effect transistor measurements carried out on ZnO films grown using identical experimental conditions yielded good

semiconducting properties, further confirming the good substrate coverage and continuity of these layers (see Section S1, Supporting Information).

3. Energy Level Quantization in Rough Semiconducting Films

Energy quantization in traditional semiconductor systems such as GaAs/AlGaAs has previously been studied via optical absorption measurements.[8] In their systems, Dingle et al. observed an optical blue shift in the absorption spectra as the semiconductor thickness was reduced.[8] Due to the very high conduction band energy of quartz, a thin layer of ZnO of thickness L, on quartz, can here be approximated by an infinite quantum well. Finite quantum well energies were also calculated using known techniques[12] (data not shown), but the results were found to be negligibly different from those evaluated using the below infinite quantum-well approximation. If we define the dimension perpendicular to the substrate surface as z, then the energy of conduction band states available to electrons confined to an infinite quantum well can be described using[13]

$$E_n = E_{xy} + \frac{n^2 h^2}{8m^* L^2} \tag{1}$$

Here, E_{xy} is the energy associated with the electron in the (unconfined) xy-plane, n is a positive integer, h is the Planck constant, m^* is the effective mass of electrons in the semiconductor, and L is the thickness of the quantum well in the z-direction. As L is reduced the energy of the first electron state ($n = 1$) and hence the conduction band minimum (CBM), increases. The energy of the first allowed transition from valance band to the conduction band similarly increases, resulting in a blue-shift in the optical absorption spectrum of the film.[8]

For semiconductors deposited via molecular-beam epitaxy (MBE) or chemical vapor deposition (CVD), the layer uniformity is extremely high and each incident photon can be assumed to encounter a single well width (L). However, since the roughness of solution-processed semiconductor layers considered here is expected to be non-negligible, it is here more appropriate to describe each incident photon as encountering a well of width L with a probability $P(\mu_L, \sigma_L)$, where μ_L is the mean well width and σ_L is the well width standard deviation. The thickness probability distribution $P(\mu_L, \sigma_L)$ is here approximated to be Gaussian (see Figure 1g for verification). In this case the probability of an incident photon encountering a well of thickness L can be described by

$$P(L, \mu_L, \sigma_L) = \frac{1}{\sigma_L \sqrt{2\pi}} \exp\left[-\frac{(L-\mu_L)^2}{2\sigma^2} \right] \tag{2}$$

The second term in Equation (1) is the energy of the quantized sub-band states in the conduction band. By substituting this into Equation (2) the probability of an incident photon encountering a well with sub-band energy levels E_n can then be described by

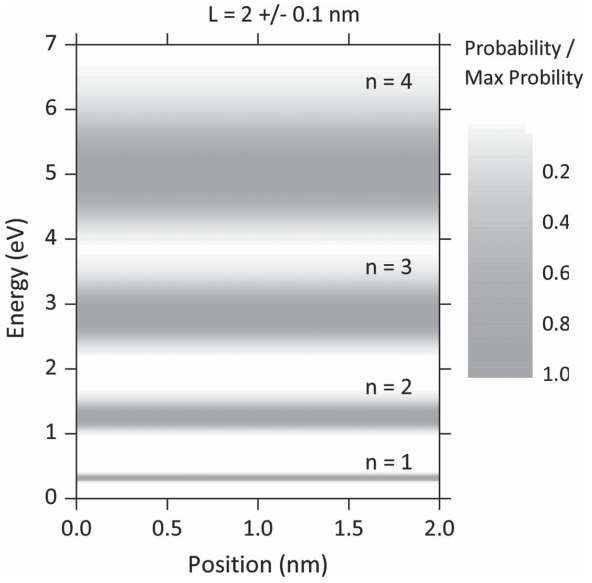

Figure 2. Probability distribution of lowest 4 energy states of infinite quantum well with a mean thickness of 2 nm, a thickness standard deviation of 0.1 nm and an effective electron mass of 0.29 m_e, evaluated using Equation (2). Darker shade represents the most likely energy for a given subband state and white represents an energy level for that state with a probability of zero.

$$P(E_n, \mu_L, \sigma_L) = \frac{1}{\sigma_L \sqrt{2\pi}} \exp\left[\frac{1}{2\sigma_L^2} \left(\frac{nh\mu_L}{\sqrt{2m^* E_n}} - \frac{n^2 h^2}{8m^* E_n} - \mu_L^2 \right) \right] \tag{3}$$

For illustrative purposes this distribution is plotted in **Figure 2** for the first four states of an infinite quantum well with $\mu_L = 2$ nm, $\sigma_L = 0.1$ nm, and $m^* = 0.29\ m_e$ (where m_e is the electron rest-mass in a vacuum). Darker areas represent the energies with the highest probability for a given n, while areas of white the energies with probability zero. Hole states in the valence band are similarly expected to be quantized, however since the hole effective mass in ZnO is significantly higher than that of electrons[14] these states have been neglected for the purposes of this study. Despite broadening, a range of energies are clearly forbidden (in particular close to the $n = 1$ subband). This illustrates that it is indeed appropriate to consider quantized carrier states in somewhat rough or nonuniform semiconductor films if the mean thickness and its standard deviation, as indicated by the rms roughness are low enough.

It should be emphasized that in the above analysis, we are specifically interested in local height variations on the order of a few nm, in contrast to large-scale nonuniformity over the area of the substrate. A Gaussian distribution is chosen (aside from empirical reasons) because it implies that the roughness is homogeneous regardless of the area studied. By extracting surface roughness values from AFM scans over small areas (such as 1 μm × 1 μm) the values can be assumed to be representative of the length scales relevant to the phenomena described above.

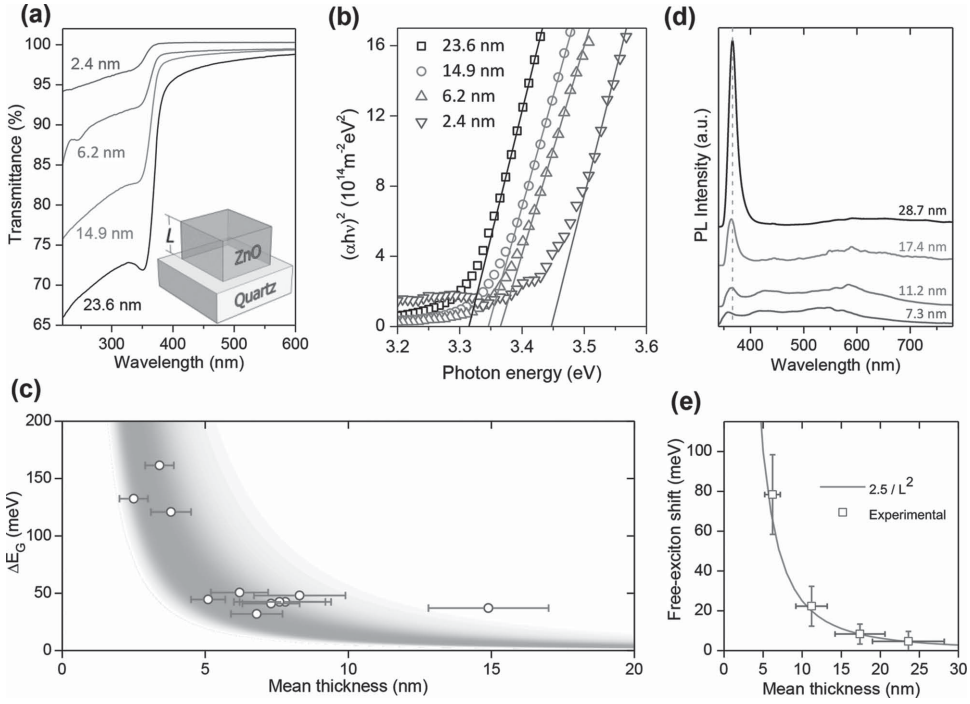

Figure 3. a) Optical transmittance spectra of four ZnO films of various thickness (L) spin-cast on quartz, corrected for reflection. b) Tauc plots of the four ZnO films from a). c) Change in optical bandgap approximated by Tauc analysis (see Section S2, Supporting Information) against mean film thickness for ten ZnO films with respect to that of bulk ZnO (here approximated as a film 23.6 nm thick). The error bars represent the standard deviation in the film thickness. The grey band illustrates the calculated change in bandgap for an infinite quantum well with a standard deviation/mean ratio of 0.2. Darker regions represents the energy with highest probability for a given mean well thickness and white represents an energy with probability zero. d) Photoluminescence (PL) spectra of four thin ZnO films of various thickness spin-cast onto polished silicon, measured at 22 K. e) Shift in exciton energy with respect to bulk ZnO (here approximated as a film 28.7 nm thick) of four thin ZnO films deposited onto polished silicon, as a function of mean film thickness. Error bars on the x-axis represent the standard deviation in the film thickness. The solid line is a plot of A/L^2 fitted to the experimental data with a prefactor of $A = 2.5$ meV nm^2.

4. Optical Characterization of ZnO Layers

To investigate the possible occurrence of energy quantization in our solution-processed oxide layers, the optical properties of several ZnO films of varying thickness were studied. **Figure 3**a shows the optical transmittance spectra of four ZnO films of varying mean thickness deposited on quartz while Figure 3b shows the respective Tauc plots.[15,16] All spectra were corrected for reflectance. As expected for quantized electron states,[8] the onset of optical absorption is blue-shifted as the average layer thickness is reduced. This effect is better illustrated in Figure 3c where the change in optical bandgap (ΔE_G)—with respect to that of bulk ZnO—of ten ZnO films is plotted as a function of average film thickness (see Section S2, Supporting Information). ZnO films with mean thickness >20 nm showed a similar bandgap of ≈3.25 eV. The latter value is approximated to be representative of bulk ZnO for the purposes of this analysis and is in good agreement with previously published results.[17] The grey band in Figure 3c illustrates the expected change in bandgap, calculated using Equation (2), with $n = 1$. When evaluating $P(\mu_L, \sigma_L)$ in Figure 3c a standard deviation was employed that was 20% of the mean film thickness for all values. This is in agreement with what was observed experimentally for the ZnO films. The effective electron mass (m^*) used was that of crystalline ZnO, i.e., $m^* = 0.29\ m_e$.[18]

We note that the effective-mass approximation has been used to calculate the expected ΔE_G despite the fact that charge transport in solution-processed metal-oxide semiconductors is often described by a hopping-like transport mechanism rather than band-like transport.[19] We therefore expect that m^* will not be constant as a function of energy. Despite this approximation a clear trend can be observed using this type of analysis, in line with an earlier (and only) report on vacuum-processed amorphous oxide superlattices.[20] Previous studies have reported a blue-shift in bulk ZnO films deposited by CVD as the growth temperature is reduced, an effect attributed to changes in material crystallinity.[21] The films studied here are known to be highly polycrystalline (see Figure 1, for example) for all layer thicknesses investigated. Similarly, phenomena such as the Burstein–Moss effect can be ruled out, as even if the semiconductor films are degenerate (transistor measurements suggest they are not—see Section S1, Supporting Information), the three-dimensional electron density is unlikely to vary substantially as a function of film thickness.

Further evidence of energy quantization in these 2-dimensional solution processed ZnO films was obtained by measuring the photoluminescence (PL) emission spectra of the ZnO as a function of layer thickness at 22 K. Ultraviolet and visible emission bands are both observed in the spectra (Figure 3d). The former is attributed to exciton emission, while the latter to defects present in ZnO, including oxygen vacancies, interstitial zinc and/or zinc vacancies. Analysis of the data reveals that the

exciton peak is blue-shifted as the mean layer thickness of ZnO is reduced, as expected for quantized carrier states.[22,23] The blue shift in the exciton peak is plotted as a function of mean film thickness in Figure 3e. As it can be seen, the films with a mean thickness of ≈28.7 nm can be assumed to be representative of bulk ZnO since for quantized systems the exciton energy is known to scale as $\approx 1/L^2$, where L is the size of the reduced dimension (i.e., layer thickness).[24] This relationship has been fitted to the experimental data in Figure 1e with a prefactor of 2.5 meV nm^{-2}. It can clearly be seen that this relation is in good agreement with the PL measurements (despite the technical challenges associated with the measurements), hence further supporting the existence of quantized states in these solution-deposited low-dimensional ZnO layers.

5. Oxide-Based Double Barrier Resonant Tunneling Devices

The existence of quantized energy states has in the past also been demonstrated through the observation of negative-differential conductance (NDC) in certain quantum well electronic device structures.[25–29] So-called double-barrier resonant tunneling diodes (RTDs) consist of a semiconducting quantum well confined between two ultrathin potential barriers, in contact with bulk semiconducting layers on either side. The bulk semiconductors are in direct contact with metal contacts [i.e., the top and bottom Al contacts in **Figure 4**a] and act as electron "reservoirs." An idealized schematic of a ZnO-based RTD is shown in Figure 4a together with the corresponding energy band diagram in equilibrium at zero bias. The operating principle of an idealized RTD under biasing is illustrated in Figure 4b,c. The quantized sub-bands confined in the center of the device act as a filter which allows the transmission of electrons at certain energies, while strongly attenuating those at other energies. When a bias (V_{Bias}) is applied across the device the chemical potential of the bulk semiconductor region on the right of the diagram (the collector) is shifted down by eV with respect to the chemical potential of the bulk semiconductor region on the left (the emitter). A linearly varying potential is then established across the device. When the quantized energy states (i.e., $n = 1$ and 2) are resonant with the occupied electron states in the emitter, the probability of an electron tunneling from left to right is enhanced. As the applied voltage increases from zero, the device current increases as the $n = 1$ state becomes resonant with the emitter layer. However, as the forward bias increases further, the device current starts decreasing since the $n = 1$ state moves below the conduction band minimum (CBM) of the emitter. Experimentally this is manifest as a region of NDC in the current–voltage characteristics.[25] This phenomenon has been observed in a range of material systems including: GaAs/AlGaAs,[25,26] InAs/AlSb,[27] Si/SiGe,[28] graphene/BN,[30] MgZnO/ZnO,[31] and single

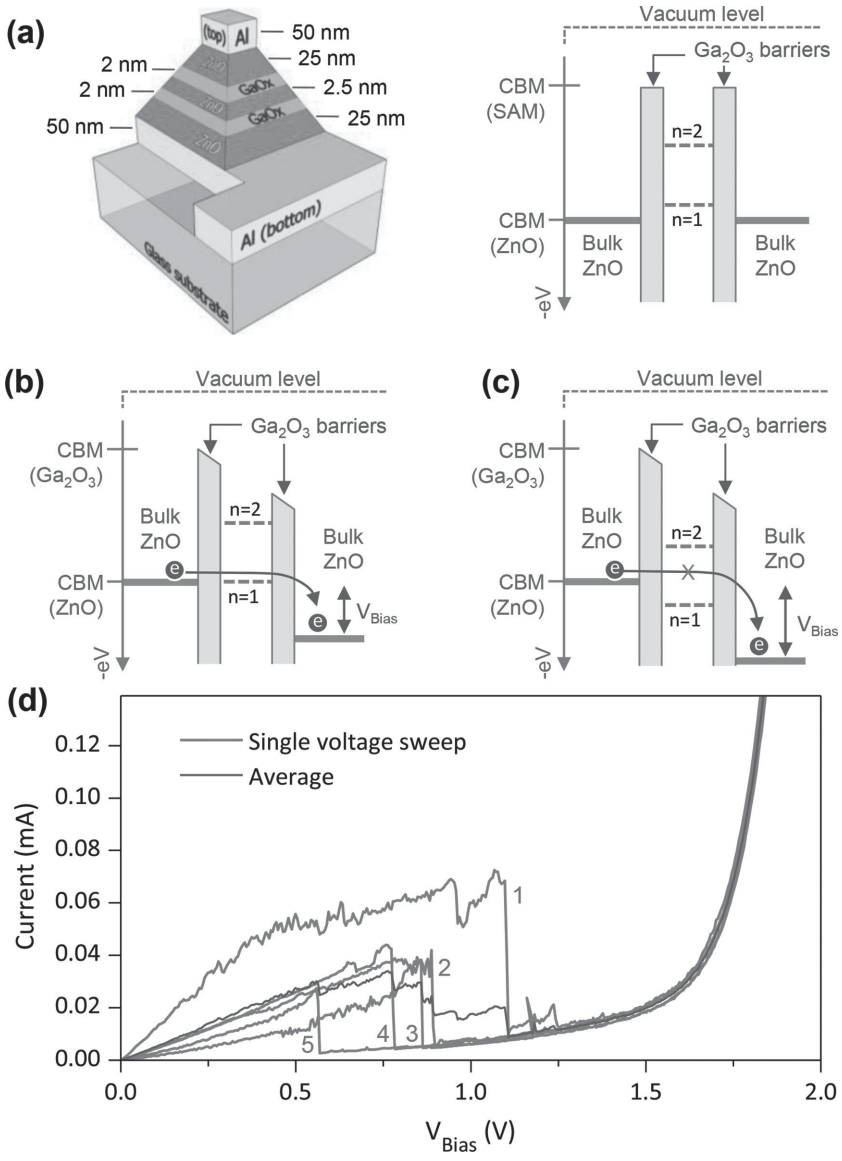

Figure 4. a) Schematic representation of the solution-processed ZnO resonant tunneling-diode (RTD) structure developed and the idealized energy band diagram under zero bias. The RTD consists of a central quantum well, formed of an ultrathin (≈2–3 nm) ZnO layer confined between two ultrathin (≈2 nm) Ga_2O_3 barrier layers. The quantum well structure is enclosed between two bulk (≈25 nm-thick) ZnO layers on either side, which are in direct-contact with aluminum electrodes (labeled Al). b,c) Idealized representation of conduction band of solution-processed resonant tunneling-diode under two biasing conditions. The labels $n = 1$ and $n = 2$ represent the discreet energy levels of the central ZnO semiconductor. The labels on the y-axis "CBM (Ga_2O_3)" and "CBM (ZnO)" represent the energies of the conduction band minima of the Ga_2O_3 barrier layers and ZnO bulk layers, respectively. d) Current–voltage characteristics of a representative RTD, measured sequentially 5 times where curve 1 represents the first voltage sweep and curve 5 the last. The blue line is the average of the five measured curves (red). The device areas were 0.64 mm^2 in each case and all measurements were carried out at room temperature under ambient pressure in nitrogen atmosphere.

molecules,[32] but to-date never in a macroscopic device based on solution-processed materials.

Aside from the academic interest related to studying the properties of quantized states, RTDs have been proposed for a range of commercial applications.[29] For example, due to their extremely fast response-time,[26,27] RTDs have been envisaged as potential high-speed signal generators and detectors.[29] Multiple-well resonant tunneling structures have also been considered as the foundations of multivalued logic circuits.[29,33] More complicated multiple quantum well structures have also been employed to create devices such as quantum-cascade lasers[34,35] and high-performance thermoelectric materials.[36] Therefore, the ability to fabricate RTD-like devices employing cost-effective manufacturing techniques on large area substrates is scientifically appealing and potentially industry-relevant.

To investigate the possibility of realizing functional resonant tunneling-like devices from solution, we fabricated RTDs using solution deposited ZnO as the bulk semiconductor and QW layers, and Ga_2O_3 [Figure 4a] as the barrier layers material (see the Experimental Section). Ga_2O_3 was chosen, first because it combines a large bandgap (≈4.9 eV) with appreciable CBM energy offset to ZnO, and second because thin layers can be grown from solution at low temperatures.[37] For the purpose of this study, the ionization potential (IP) and valence band maxima (VBM) for both metal oxides were determined by ultraviolet photoelectron spectroscopy (UPS), respectively. The CBM energies for ZnO and Ga_2O_3 calculated were ≈3.8 and ≈2.8 eV, respectively, in agreement with previously published data. The potential barrier height in the conduction band of the Ga_2O_3/ZnO/Ga_2O_3 quantum well was therefore approximated to be ≈1.0 eV. Figure 4d shows the current–voltage (*I*–*V*) characteristics of a representative device measured repeatedly 5 times. Qualitatively similar *I*–*V* curves were obtained for 100 s of devices processed in parallel. In each case electrical characterization was carried out at room temperature in ambient-pressure under nitrogen atmosphere. Despite the difference among the subsequent voltage sweeps, there is a clear region of NDC observable in this device. The variation in the voltage at which NDC occurs is likely to be due to charging/discharging effects owed to the presence of electron traps- and/or material instability including ionic migration and/or polarization effects.[38,39] Furthermore, significant operating hysteresis was observed between the forward and reverse bias sweeps (data not shown) making detailed analysis of the NDC voltage region very challenging.

In order to rule out other possible mechanisms that could give rise to NDC phenomena, we fabricated a series of control devices in parallel to the RTD devices shown in Figure 4a. For each control device the deposition of the two Ga_2O_3 barrier layers was omitted during device fabrication, leading to the formation of the two-terminal ZnO device shown in **Figure 5**a, with an approximate semiconductor thickness of 50 nm. Out of

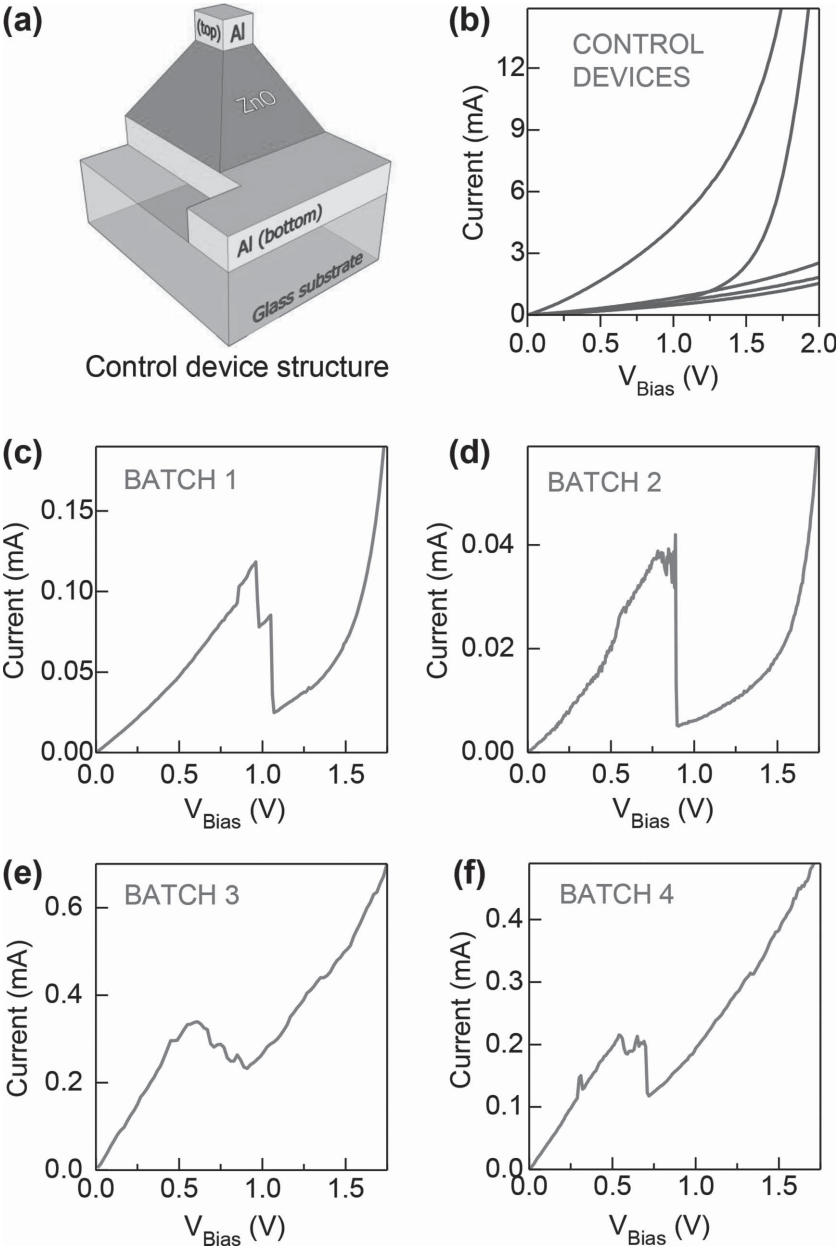

Figure 5. a) Schematic representation of the control device structure developed. b) Representative current-voltage characteristics of five example control devices, fabricated in parallel to the RTDs measured in Figure 4, but with the two Ga_2O_3 deposition steps omitted. The ZnO layer thickness used in all control devices was approximately 50 nm. c–f) Representative current–voltage characteristics measured for four different Ga_2O_3-based resonant-tunneling diodes prepared in four different batches on different dates. All RTDs consist of a central quantum well formed of an ultrathin (≈2–3 nm) ZnO layer sandwiched between two ultrathin (≈2 nm) Ga_2O_3 barrier layers. Device areas were 0.64 mm^2 in each case and all measurements were carried out under ambient pressure in nitrogen.

over 40 control devices measured from the same batch, not a single *I–V* exhibited anything resembling NDC. A plot of representative *I–V* characteristics measured from five different control devices is shown in Figure 5b. Similarly, control devices based on a single Ga_2O_3 barrier layer also failed to yield *I–V* characteristics with the NDC feature present. In parallel to the control devices, four separate batches of RTDs [Figure 4a] were fabricated on different dates and electrically characterized using identical experimental conditions. Figure 5c–f display representative *I–V* curves measured from different devices. On each occasion the two-terminal devices exhibited clear NDC regions occurring at comparable bias levels, with peak-to-valley current ratios in the range 2–7. The peak current-density recorded just before the NDC region was also found to vary with typical values in the range 5–50 mA cm^{-2}. This variation is most likely attributed to the difference in the effective active area between devices (that is the area of the device that exhibits resonant tunneling conduction) due to the non-uniform layer thickness of key device components such as the ZnO quantum well and the tunneling barriers (i.e., Ga_2O_3) width. Such nonuniformities could well lead to reduction of resonant tunneling events and hence to a significant variation in the peak tunneling current between devices. Studies focusing on mapping the resonant tunneling regions across the geometrical area of the RTDs using the current-AFM techniques are presently underway and will be reported in the future.

Despite the variation in the operating characteristics between different RTDs, as-prepared devices could be stored for several days under ambient N_2, after which the NDC feature remained measureable—a feature indicative of the good stability of these devices when not in operation. Despite theoretical predictions, however, the NDC feature was generally only observable in the first quadrant of the *I–V* plot and only in a few devices it appeared in the third quadrant. We attribute this to the fact that although conceptually the device structure in Figure 4a appears symmetric, in reality the bottom Al/ZnO(bulk) interface and the top ZnO(bulk)/Al interfaces are expected to be substantially different due to the specific fabrication steps used (e.g., exposure of bottom Al electrode to sequential spin-casting of ZnO layers and thermal annealing steps during layer growth). This characteristic "asymmetry" in the device structure is believed to be the most likely reason for the absence of NDC in the third quadrant of *I–V* characteristics.

Negative differential conductance has previously been observed in resistance random-access memory devices and was attributed to the migration of oxygen vacancies.[40,41] Although we cannot rule out this as a possibility, given the absence of any NDC-like feature in our control devices in combination with the clear signatures of quantized energy states in thin ZnO films obtained via optical spectroscopy measurements (Figure 3) and the improved data sets that will be discussed in Section 6 for hybrid RTDs, we argue that the NDC feature presented in Figure 4d and Figure 5c–f being due to a resonant tunneling process is a more-likely explanation, and certainly a concept worthy of further investigation.

The maximum peak-to-valley current ratio measured from these RTDs was relatively high and on the order of ≈7. The peak current before the region of NDC occurred at voltages in the range 0.6–1.1 V. This peak current is expected to occur at a voltage approximately twice the energy of the peak electron transmittance divided by the electron charge (*e*).[25] By employing a basic model developed for traditional RTDs,[42] the first peak transmittance in this device was approximated to occur at 0.12 eV. Therefore, NDC is expected to occur at around 0.24 V bias—approximately 2 to 4 times lower than the experimentally measured voltages (see Section S3, Supporting Information). These larger than expected voltages are likely to be due to applied potential being dropped elsewhere across the device structure. For example, a high-resistance layer of Al_2O_3 is known to form between ultrathin layers of ZnO and evaporated top Al electrodes after thermal annealing.[6] The presence of such electrically insulating layer(s) among other parasitic effects, are therefore expected to introduce significant deviations from the ideal device structure considered in the model. Furthermore, applying the model to a system formed between asymmetrically rough semiconductors/electrodes is also likely to introduce substantial differences in the predicated device operation.

6. Hybrid Resonant Tunneling Devices

In an attempt to improve the device performance and also simplify the manufacturing process, we fabricated ZnO-based devices using insulating organic self-assembled monolayers (SAM) as the tunneling barrier materials. Two types of organic molecules were investigated, namely hexamethyldisilazane (HMDS) and phosphonohexadecanoic acid (PHDA) [**Figure 6**a]. Both SAM molecules are known to form dense and conformal self-assembled monolayers on solid surfaces with suitable chemistry[43–46] and have been used extensively as surface passivation agents,[47] surface energy modifiers,[45,48] and ultrathin gate dielectrics in low-voltage organic transistors.[45] Importantly, both SAMs can be processed from solution or vapor phase at room temperature onto large-area substrates and the resulting monolayers are known to exhibit excellent thermal stability making them compatible with the device process flowchart employed in this work.[49] Similar to Ga_2O_3, HMDS and PHDA exhibit large bandgaps and as such are expected to give rise to multiple-eV quantum wells when incorporated as the barrier systems in ZnO quantum well-based RTDs. Unlike epitaxially-grown and solution-grown tunneling barriers, however, the combination of the well-defined chemical structure (molecular length) and self-assembling character (defined by the anchoring chemical group used) of the SAMs enables control of the barrier width down to atomic dimensions through simple chemistry and highly scalable wet-based deposition techniques.

Figure 6b displays a schematic representation of the SAM-based device structure developed, while Figure 6c shows the idealized energy band diagram of the device under equilibrium at zero bias. Representative sets of the *I–V* characteristics measured for two devices based on HMDS and PHDA barrier layers are shown in Figure 6d,e, respectively. Here, five sets of *I–V* characteristics were recorded sequentially from each device at room temperature. Both types of hybrid RTDs show

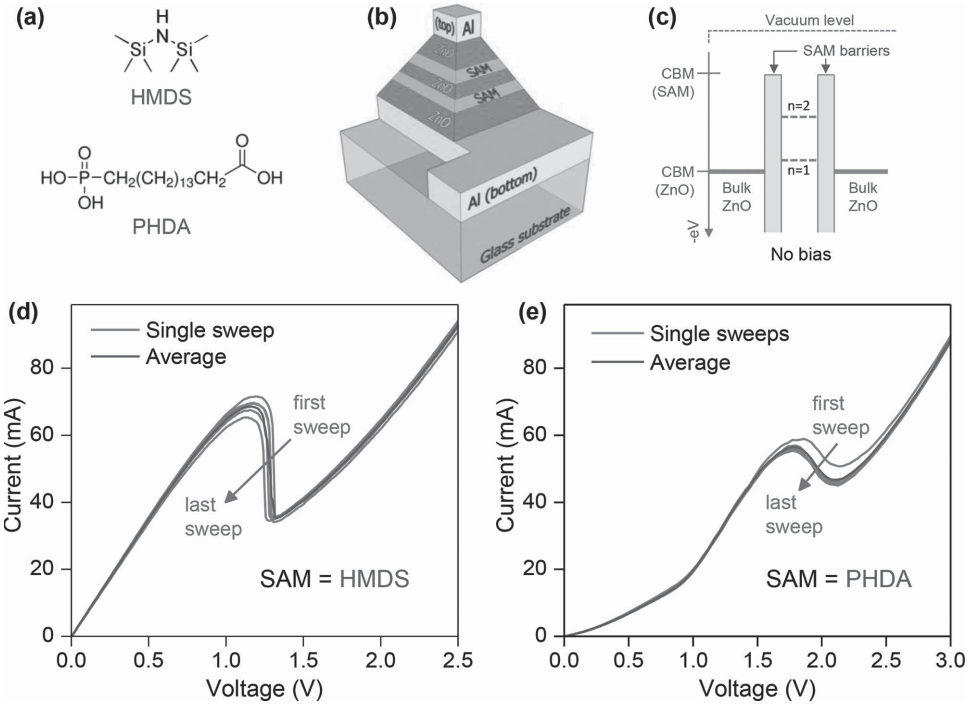

Figure 6. a) Molecular structures of the organic barrier molecules hexamethyldisilazane (HMDS) and phosphonohexadecanoic acid (PHDA). b) Schematic representation of solution-processed ZnO resonant tunneling-diode (RTD) structure employing self-assembled monolayer (SAM) barriers. The structure is identical to that of Figure 4a) but with the Ga_2O_3 barriers being replaced by the SAM layers. c) Idealized representation of conduction band of a SAM-based RTD without any bias. The labels on the *y*-axis "CBM (SAM)" and "CBM (ZnO)" represent the energies of the conduction band minima of the SAM barrier monolayers and ZnO bulk layers, respectively. Representative current–voltage characteristics measured for RTDs based on the barrier layers of d) HMDS and e) PHDA, measured sequentially 5 times. The blue line is the average of the five *I–V* characteristics (red curves). Each RTD consists of a 2–3 nm-thick ZnO quantum well confined between the two SAM barriers. The device areas were 0.64 mm^2 in each case and all measurements were carried out at room temperature under ambient pressure in nitrogen atmosphere.

well-defined NDC regions with peak-to-valley ratios in the range 1–2. The peak current densities measured just before the NDC region was on the order of 10 A cm^{-2} for both types of devices and were recorded at around ≈1.2 V for PHDA and at ≈1.8 V for HMDS-based RTDs. The latter value is significantly lower than current densities reported for traditional RTDs (typically in the range 0.5–10 kA cm^{-1}) based on AlGaAs/GaAs, InAs/AlSb, InGaAs/AlAs/InAs, etc.[25,27,50] We attribute this to a number of factors that include, the significantly lower electron mobility of the polycrystalline ZnO [Figure S1(c), Supporting Information] and the presence of inactive device regions, i.e., parts of the apparent device area that do not exhibit resonant tunneling conduction due to quantum well/barrier layer thickness variations.

The higher voltages with respect to those measured in the Ga_2O_3-based ZnO RTDs is in agreement with a deeper quantum well,[42] resulting from the wide bandgap nature of these SAMs. Although the structural quality of our devices is not expected to be comparable in terms of uniformity to epitaxially grown RTDs, the use of conformal SAM barriers in combination with solution processed low-dimensional ZnO QWs appears to yield functional devices with operating characteristics closely resembling those of state-of-the-art GaAs/AlGaAs double-barrier RTDs.[26] The improved electrical stability of the SAM-based (hybrid) ZnO RTDs with respect to Ga_2O_3 based devices is attributed to the conformal nature of the SAM molecules. In the case of Ga_2O_3 barriers, certain intermixing between ZnO and Ga_2O_3 may take place leading to non-idealities in the barrier profile while the Ga_2O_3 barriers themselves are likely to exhibit structural roughness. On the contrary, SAM barriers are characterized by an extremely well-defined chemical structure and hence molecular length (i.e., barrier thickness) that is typically below 3 nm depending on the molecule used. Because of these unique characteristics, incorporation of organic SAMs as the tunneling barriers is expected to have a negligible impact on interfaces' roughness and stoichiometry.

Finally, we note that the qualitative difference in the form of the *I–V* curves measured from RTDs employing Ga_2O_3 barriers and those employing SAM barriers is a persistent characteristic of all devices measured in this study. We thus believe that the nature of the tunneling barriers is the primary reason for this observation and potentially a key to further developments. However, an in-depth study into the nature of this difference is beyond the scope of this work and will be the focus of future investigations.

7. Conclusions

We have presented strong evidence of the existence of quantized energy states in ultrathin layers of ZnO processed from solution at ≤200 °C in air. In agreement with experiments

carried out using traditional quantum well systems (e.g., GaAs/AlGaAs)[8], we observe a widening of the optical band gap of ZnO layers as the mean thickness is reduced, accompanied by a blue shift in the λ_{MAX} of the photoluminescence signal. By combining these solution-processed ZnO layers with Ga_2O_3 or organic self-assembled monolayers as tunneling barrier materials, two terminal devices with current–voltage characteristics resembling those of traditional double barrier resonant tunneling diodes were fabricated. The devices were observed to exhibit reproducible negative differential conductivity at room temperature with peak-to-valley ratios in the range 2–7. The ability to grow from solution and at plastic-compatible temperatures (≤200 °C) complex heterostructures with nanoscale accuracy, and the demonstration of what appear to be functional resonant tunneling diodes with performance characteristics comparable to traditional GaAs/AlGaAs devices,[26] creates new opportunities for both basic research and various technological applications.

8. Experimental Section

Solution Preparation and Processing: ZnO hydrate ($ZnO{\cdot}xH_2O$) was dissolved in ammonium hydroxide at a variety of concentrations. Gallium nitrate hydrate ($Ga(NO_3)_3xH_2O$) was dissolved in deionized water at a concentration of 12 mg mL^{-1}. Solutions were stirred overnight at room temperature before deposition. Solutions of phosphonohexadecanoic acid (PHDA) were prepared in IPA at a concentration of 50 mg/30 mL. Hexamethyldisilazane (HMDS) was purchased in solution and used as received. All materials are commercially available and were obtained from Sigma-Aldrich (UK).

High-Resolution Transmission Electron Microscopy (HRTEM): A transmission electron microscope operating at an accelerating voltage of 300 kV (Titan 80–300 Super Twin, FEI Company) was used to acquire cross-section micrographs. Charged couple device (CCD) camera (Model: US4000, Gatan Inc.) was used to record HR-TEM images. Samples were prepared on a focused ion beam (FIB; Helios 400s, FEI) equipped with a nanomanipulator (Omniprobe, AutoProbe300) with lift-out method. Electron beam assisted carbon and platinum deposition was performed on the sample surface to protect the thin film surface against the ion beam bombardment during ion beam milling. Ga ion beam (30 kV, 9 nA) was first used to cut the sample from the bulk (30 kV, 9 nA), after which it was attached to a Cu grid using a lift-out method. The sample was subsequently thinned down to ≈50 nm thickness (30 kV, 93 pA) and cleaned (2 kV, 28 pA) to get rid of areas of the sample damaged during the thinning process.

Grazing Incident X-Ray Diffraction (GID): Grazing incident X-ray diffraction measurements were carried out on beamline G2 in Cornell High Energy Synchrotron Source (CHESS), Cornell University. The samples were aligned on a Kappa diffractometer with the X-ray energy of 13.65 keV (λ = 0.0908 nm) through a Be single-crystal monochromator. The data was collected using a 640-element 1D diode-array detector, with a set of 0.1° Soller slits mounted on the detector arm to provide an in-plane resolution of 0.16°. The grazing incident angle was fixed at 0.1° in GID.

Atomic Force Microscopy (AFM): Atomic force microscopy was carried out in tapping mode using an Agilent 5500 atomic force microscope in ambient atmosphere. The approximate resonance frequency of the cantilever was 250 kHz and the force constant was approximately 60 Nm^{-1}.

Optical Transmittance Measurements: ZnO films were spin-cast onto quartz substrates from the solutions described above in air. The films were then annealed at 200 °C for 30 min in air. Measurements were carried out with a Shimadzu UV-2600 UV–vis spectrophotometer. Transmittance and reflectance measurements were carried out for each sample. The transmittance corrected for reflectance was derived from the raw transmittance + raw reflectance.

Photoluminescence Measurements: ZnO films were spin-cast onto polished silicon in air. The films were annealed at 200 °C for 30 min in air. Low temperature photoluminescence (PL) spectra of the films were excited by a 35 mW He–Cd continuous wave laser emitting at 325 nm. The measurements were performed at 22 K in high vacuum and the recorded spectra were resolved using a spectrometer with an UV grating of 600 grooves mm^{-1} and a sensitive, calibrated liquid nitrogen cooled CCD camera.

Resonant Tunneling Diodes Fabrication: All two-terminal resonant tunneling diode (RTD)-like structures were fabricated on glass substrates. In brief; 50 nm-thick aluminum bottom electrodes were deposited via thermal evaporation under high vacuum through shadow masks at an average rate of 0.5 Å s^{-1}. A bulk ZnO layer was deposited by five sequential spin-casting and thermal annealing steps. Each spin-casting step was followed by an annealing step at 200 °C for 30 min in air. Next a barrier layer was deposited on top of the bottom bulk ZnO layer. Three different materials were employed as tunneling barriers in three different sets of devices. For Ga_2O_3-based devices, a single layer of Ga_2O_3 was spin-cast from gallium nitrate hydrate solution in air. The samples were then annealed at 200 °C for 30 min in air. For the second set of devices, HMDS was applied as a barrier layer. This was applied by placing the samples in vapor-phase HMDS at 80 °C for 30 min. Finally, a monolayer of PHDA was applied to the third set of devices by submerging the samples in PHDA solution for 90 min each. The PHDA-based samples were then thoroughly rinsed in IPA before being annealed in nitrogen at 90 °C for 30 min. A single ultrathin layer of ZnO was then spin-cast onto the predeposited tunneling barrier layer acting as the quantum well. The layer thickness of the ZnO quantum well was estimated to be on the order of ≈2.4 nm and was controlled by tuning the concentration of the precursor solution and spinning speed during depositing. A second barrier layer of either Ga_2O_3, HMDS, or PHDA was then applied on top of the thin ZnO layer in an identical manner as described above. A second bulk ZnO layer was deposited directly onto the second barrier layer via five-sequential spin-castings/thermal annealing steps, as described above for the bottom bulk ZnO layer. Finally, 50 nm-thick aluminum top electrodes were deposited via thermal evaporation under high vacuum through shadow masks at an average rate of 0.5 Å s^{-1}. Electrical characterization was carried out at room temperature under ambient pressure in nitrogen using an Agilent B2902A semiconductor parameter analyzer. The geometrical area of as-prepared devices was 0.64 mm^2.

X-Ray Photoelectron Spectroscopy and Ultraviolet Photoelectron Spectroscopy: Surface analysis studies were performed in an ultrahigh vacuum system (UHV) which consists of a fast entry specimen assembly, a sample preparation, and an analysis chamber equipped with a SPECS LHS-10 hemispherical electron analyzer. The base pressure in both chambers was 1×10^{-9} mbar. Unmonochromatized AlKα line at 1486.6 eV and an analyzer pass energy of 36 eV, giving a full width at half maximum (FWHM) of 0.9 eV for the Au $4f_{7/2}$ peak, were used in all X-ray photoelectron spectroscopy (XPS) measurements. The analyzed area was an ellipse with dimensions 2.5 mm × 4.5 mm. The XPS core level spectra were analyzed using a fitting routine, which can decompose each spectrum into individual mixed Gaussian-Lorentzian peaks after a Shirley background subtraction. The samples were measured as received. The main C1s peak at 284.8 eV from superficial carbon was used in binding energy (BE) corrections for specimen charging. The ultraviolet photoelectron spectroscopy (UPS) spectra were obtained using HeI irradiation with $h\nu$ = 21.23 eV produced by an UV source (model UVS 10/35). During UPS measurements the analyzer was working at the Constant Retarding Ratio (CRR) mode, with CRR = 10. The work function (Φ) was determined from the UPS spectra by subtracting their width (i.e., the energy difference between the analyzer Fermi level and the high binding energy cut-off), from the HeI excitation energy. For these measurements a bias of –12.29 V was applied to the

sample in order to avoid interference of the spectrometer threshold in the UPS spectra.

Supporting Information

Supporting Information is available from the Wiley Online Library or from the author.

Acknowledgements

J.G.L., Y.-H.L., J.S., and T.D.A. are grateful to Dutch Polymer Institute (DPI) S-PLORE Grant No. 735 and European Research Council (ERC) AMPRO Project No. 280221 for financial support. CHESS is supported by the NSF & NIH/NIGMS via NSF Award No. DMR-1332208.

Received: November 2, 2014
Revised: December 28, 2014
Published online: February 13, 2015

[1] E. Fortunato, P. Barquinha, R. Martins, *Adv. Mater.* **2012**, *24*, 2945.
[2] S. R. Thomas, P. Pattanasattayavong, T. D. Anthopoulos, *Chem. Soc. Rev.* **2013**, *42*, 6910.
[3] K. Ghaffarzadeh, R. Das, http://www.idtechex.com/research/reports/metal-oxide-tft-backplanes-for-displays-2013–2018-analysis-trends-forecasts-000334.asp? (accessed: January 2015).
[4] K. K. Banger, Y. Yamashita, K. Mori, R. L. Peterson, T. Leedham, J. Rickard, H. Sirringhaus, *Nat. Mater.* **2011**, *10*, 45.
[5] R. Theissmann, S. Bubel, M. Sanlialp, C. Busch, G. Schierning, R. Schmechel, *Thin Solid Films* **2011**, *519*, 5623.
[6] Y.-H. Lin, H. Faber, K. Zhao, Q. Wang, A. Amassian, M. McLachlan, T. D. Anthopoulos, *Adv. Mater.* **2013**, *25*, 4340.
[7] J. S. Lee, Y.-J. Kwack, W.-S. Choi, *J. Korean Phys. Soc.* **2011**, *59*, 3055.
[8] R. Dingle, W. Wiegmann, C. H. Henry, *Phys. Rev. Lett.* **1974**, *33*, 827.
[9] G. Adamopoulos, A. Bashir, W. P. Gillin, S. Georgakopoulos, M. Shkunov, M. A. Baklar, N. Stingelin, D. D. C. Bradley, T. D. Anthopoulos, *Adv. Funct. Mater.* **2011**, *21*, 525.
[10] A. I. M. Rae, *Quantum Mechanics*, Taylor & Francis Group, New York **2008**.
[11] Y. H. Lin, H. Faber, J. G. Labram, E. Stratakis, L. Sygellou, E. Kymakis, N. A. Hastas, L. R., K. Zhao, A. Amassian, N. D. Treat, M. McLachlan, T. D. Anthopoulos, unpublished.
[12] C. Weisbuch, B. Vinter, *Quantum Semiconductor Structures: Fundamentals and Applications*, Academic Press, San Diego, CA **1991**.
[13] J. R. Hook, H. E. Hall, *Solid State Physics*, Wiley, Chichester, UK **1991**.
[14] B. Enright, D. Fitzmaurice, *J. Phys. Chem.* **1996**, *100*, 1027.
[15] J. Tauc, R. Grigorovici, A. Vancu, *Phys. Status Solidi B* **1966**, *15*, 627.
[16] J. Tauc, *Mater. Res. Bull.* **1968**, *3*, 37.
[17] Y. Xu, M. A. A. Schoonen, *Am. Mineral.* **2000**, *85*, 543.
[18] W. S. Baer, *Phys. Rev.* **1967**, *154*, 785.
[19] F. Torricelli, J. R. Meijboom, E. Smits, A. K. Tripathi, M. Ferroni, S. Federici, G. H. Gelinck, L. Colalongo, Z. M. Kovacs-Vajna, D. de Leeuw, E. Cantatore, *IEEE Trans. Electron Devices* **2011**, *58*, 2610.
[20] K. Abe, K. Nomura, T. Kamiya, H. Hosono, *Phys. Rev. B* **2012**, *86*, 081202.
[21] S. T. Tan, B. J. Chen, X. W. Sun, W. J. Fan, H. S. Kwok, X. H. Zhang, S. J. Chua, *J. Appl. Phys.* **2005**, *98*, 013505.
[22] A. A. Mosquera, D. Horwat, A. Rashkovskiy, A. Kovalev, P. Miska, D. Wainstein, J. M. Albella, J. L. Endrino, *Sci. Rep.* **2013**, *3*, 1714.
[23] C. Dang, J. Lee, C. Breen, J. S. Steckel, S. Coe-Sullivan, A. Nurmikko, *Nat. Nanotechnol.* **2012**, *7*, 335.
[24] L. E. Brus, *J. Chem. Phys.* **1984**, *80*, 4403.
[25] L. L. Chang, L. Esaki, R. Tsu, *Appl. Phys. Lett.* **1974**, *24*, 593.
[26] T. C. L. G. Sollner, W. D. Goodhue, P. E. Tannenwald, C. D. Parker, D. D. Peck, *Appl. Phys. Lett.* **1983**, *43*, 588.
[27] E. Ozbay, D. M. Bloom, D. H. Chow, J. N. Schulman, *IEEE Electron Device Lett.* **1993**, *14*, 400.
[28] K. Ismail, B. S. Meyerson, P. J. Wang, *Appl. Phys. Lett.* **1991**, *59*, 973.
[29] H. Mizuta, T. Tanoue, *The Physics and Applications of Resonant Tunnelling Diodes*, Cambridge University Press, Cambridge, UK **2006**.
[30] L. Britnell, R. V. Gorbachev, A. K. Geim, L. A. Ponomarenko, A. Mishchenko, M. T. Greenaway, T. M. Fromhold, K. S. Novoselov, L. Eaves, *Nat. Commun.* **2013**, *4*, 1794.
[31] S. Krishnamoorthy, A. A. Iliadis, A. Inumpudi, S. Choopun, R. D. Vispute, T. Venkatesan, *Solid-State Electron.* **2002**, *46*, 1633.
[32] J. Chen, M. A. Reed, A. M. Rawlett, J. M. Tour, *Science* **1999**, *286*, 1550.
[33] J. L. Huber, J. Chen, J. A. McCormack, C. W. Zhou, M. A. Reed, *IEEE Trans. Electron Devices* **1997**, *44*, 2149.
[34] J. Faist, F. Capasso, D. L. Sivco, C. Sirtori, A. L. Hutchinson, A. Y. Cho, *Science* **1994**, *264*, 553.
[35] B. S. Williams, *Nat. Photonics* **2007**, *1*, 517.
[36] L. D. Hicks, M. S. Dresselhaus, *Phys. Rev. B* **1993**, *47*, 12727.
[37] S. R. Thomas, G. Adamopoulos, Y.-H. Lin, H. Faber, L. Sygellou, E. Stratakis, N. Pliatsikas, P. A. Patsalas, T. D. Anthopoulos, *Appl. Phys. Lett.* **2014**, *105*, 092105.
[38] A. Janotti, C. G. Van de Walle, *Phys. Rev. B* **2007**, *76*, 165202.
[39] A. Dal Corso, M. Posternak, R. Resta, A. Baldereschi, *Phys. Rev. B* **1994**, *50*, 10715.
[40] Y. Li, S. Long, Q. Liu, H. Lü, S. Liu, M. Liu, *Chin. Sci. Bull.* **2011**, *56*, 3072.
[41] S. Nigo, M. Kubota, Y. Harada, T. Hirayama, S. Kato, H. Kitazawa, G. Kido, *J. Appl. Phys.* **2012**, *112*, 033711.
[42] R. Tsu, L. Esaki, *Appl. Phys. Lett.* **1973**, *22*, 562.
[43] M. L. Hair, W. Hertl, *J. Phys. Chem.* **1971**, *75*, 2181.
[44] R. Anwander, I. Nagl, M. Widenmeyer, G. Engelhardt, O. Groeger, C. Palm, T. Röser, *J. Phys. Chem. B* **2000**, *104*, 3532.
[45] J. M. Ball, P. H. Wobkenberg, F. Colleaux, M. Heeney, J. E. Anthony, I. McCulloch, D. D. C. Bradley, T. D. Anthopoulos, *Appl. Phys. Lett.* **2009**, *95*, 103310.
[46] M. Novak, T. Schmaltz, H. Faber, M. Halik, *Appl. Phys. Lett.* **2011**, *98*, 093302.
[47] L.-L. Chua, J. Zaumseil, J.-F. Chang, E. C. W. Ou, P. K. H. Ho, H. Sirringhaus, R. H. Friend, *Nature* **2005**, *434*, 194.
[48] S. C. Lim, S. H. Kim, J. H. Lee, M. K. Kim, D. J. Kim, T. Zyung, *Synth. Methods* **2005**, *148*, 75.
[49] A. Bashir, P. H. Wöbkenberg, J. Smith, J. M. Ball, G. Adamopoulos, D. D. C. Bradley, T. D. Anthopoulos, *Adv. Mater.* **2009**, *21*, 2226.
[50] C. I. Huang, M. J. Paulus, C. A. Bozada, S. C. Dudley, K. R. Evans, C. E. Stutz, R. L. Jones, M. E. Cheney, *Appl. Phys. Lett.* **1987**, *51*, 121.